CFD simulation of methanation reaction over 3D-printed monolithic catalysts: A comparative study

Mingzheng Zhang[1], Michelle Ng Xin Yi[2], Ban Zhen Hong[2], Liming Che[1], Binghui Chen[1,2]

[1] *Department of Chemical & Biochemical Engineering, College of Chemistry & Chemical Engineering, Xiamen University, Xiamen 361005, P. R. China*

[2] *School of Energy & Chemical Engineering, Xiamen University Malaysia, Sepang 43900, Malaysia*

Correspondence:

Ban Zhen Hong, School of Energy & Chemical Engineering, Xiamen University Malaysia, Sepang 43900, Malaysia, bzhong@xmu.edu.my

Liming Che, Department of Chemical & Biochemical Engineering, Xiamen University, Xiamen 361005, P. R. China, lmc@xmu.edu.cn

Binghui Chen, Department of Chemical & Biochemical Engineering, Xiamen University, Xiamen 361005, P. R. China, chenbh@xmu.edu.cn

Abstract

Exothermic methanation reaction from syngas to synthetic natural gas (SNG) in fixed-bed reactor suffers from hot-spot formation caused by limited heat transfer area and relatively poor radial heat transfer of catalyst particle packings. To address this issue, monolithic catalyst with excellent transport and mechanical properties is under development. In this contribution, CFD simulations of methanation reaction from syngas to SNG over three types of 3D-printed monolithic catalysts were performed. The simulation results are in good agreement with experimental ones. Compared with monolithic catalyst with honeycomb-shaped straight-channel structure or tetrahedral periodic structure, bio-inspired monolithic catalyst having the same characteristic of cancellous bone was found to be promising due to its lower pressure drop, better heat transfer, superior mass transfer and thus higher conversion of syngas. The mechanism and promising applications of 3D-printing bio-inspired monolithic catalyst are discussed.

Keywords: 3D-printing, cancellous bone, CFD simulation, methanation reaction, monolithic catalyst

1. INTRODUCTION

In chemical industry, catalysts are usually packed in reactor in the form of pellets.[1] Fixed-bed reactor has excellent mass transfer property and flow pattern close to plug flow. While the disadvantages of fixed-bed reactor are high flow resistance (pressure drop) and thermal resistance (poor heat transfer).[2,3] For strong exothermic reactions, such as methanation reaction from syngas to synthetic natural gas (SNG), high flow resistance and thermal resistance may lead to the formation of hot-spots in the fixed-bed reactor, resulting in catalyst deactivation and formation of unexpected byproduct.[4]

In order to overcome the aforementioned problems, monolithic catalyst is under development. Monolithic catalyst with honeycomb-shaped straight channels was initially applied in catalytic oxidation of automotive exhausts.[5] Honeycomb-type monolithic catalyst is prepared by extrusion method and widely applied due to the simplicity of preparation process.[6] Compared to pelleted catalysts in fixed-bed reactor, honeycomb-type monolithic catalyst reduces the flow resistance effectively.[7] However, honeycomb-type monolithic catalyst has similar adverse effect for exothermic reactions due to the absence of radial mass and heat transfer.[8] The introduction of tortuous channels into monolithic catalyst is considered as a solution as such pathways promote radial mass and heat transfer.[7,9] Therefore, monolithic catalyst integrated with tortuous channels might be an better alternative to pelleted catalysts.[8] The problem of monolithic catalysts with tortuous channels is that it is extremely difficult to prepare by using conventional extrusion method.

Three-dimensional (3D) printing, also known as additive manufacturing, is a “bottom-up” layer-by-layer printing technique which can be used to build complex structures that are

difficult to prepare by using conventional extrusion method.[6,10-12] The preparation of monolithic catalysts with complex structures by 3D printing has received much attention in the past decade.[13-19] Li et al.[16] prepared monolithic catalysts with different channel architectures by the self-sacrifice template method and found that monolithic catalyst with tetrahedral periodic channel has the highest catalytic activity. Quintanilla et al.[17] prepared Fe/SiC monolithic catalyst by 3D printing and then evaluated its activity and stability in catalytic wet peroxide oxidation of phenol. Li et al.[18] prepared a series of ZSM-5 monolithic catalysts doped with Cr, Cu, Ga, La, Mg, Y, and Zn by 3D-printing and then tested their catalytic performance in the methanol to olefins reaction. Azuaje et al.[19] employed the 3D-printing approach to synthesize a reusable alumina monolithic catalyst, which improved the conversion in synthesis of bioactive 3,4-dihydropyrimidin-2(1*H*)-one and 1,4-dihydropyridine. In the reports mentioned above, the majority of 3D-printed monolithic catalysts had regular periodic structures. On the contrary, monolithic catalysts with irregular pore structures received very few attentions.

There are countless irregular pore structures in nature. Among them, cancellous bone has received extensive attention due to its superior mechanical properties.[20-22] The multi-scale porous structure of cancellous bone might be more conducive to mass and heat transfer when used as a monolithic catalyst.[23,24] The multi-scale porous structure and broad spectra of curvature of pore surface may show advantages on catalytic activity and hydrodynamics. Therefore, incorporating the structure of cancellous bone into monolithic catalyst might have favorable effects on catalytic performance.[25-27]

In order to prepare a monolithic catalyst having the same characteristic of cancellous

bone, micro X-ray computed tomography (μ-CT) can be used. μ-CT is commonly employed for the visualization of plant and animal tissues, which enables 3D reconstruction of irregular pore structures.[28,29] By combining μ-CT with 3D printing, it becomes realistic to prepare a monolithic catalyst with irregular pore structure.

In the present work, methanation reaction from syngas to SNG over 3D-printed monolithic catalysts was simulated using CFD. Performances of monolithic catalysts with different pore structures, i.e., honeycomb-type structure with straight channels, periodic tetrahedral structure with regular tortuous channels and the structure of cancellous bone with irregular pores are compared. The aim is to find a porous structure with superior catalytic activity and interpret the underneath mechanism.

2. METHODOGY

2.1 Preparation of cancellous bone from bovine humerus

Fresh bovine humerus was obtained from local market. A trephine was then used to drill at the end of the bovine humerus to obtain a cylindrical specimen of cancellous bone with a diameter of 4 mm and a height of 9 mm. To facilitate the subsequent μ-CT scanning, the specimen was immersed in trichloroethylene for 72 h to degrade and remove the marrow. The as-prepared specimen of cancellous bone from bovine humerus is shown in Figure 1a & b.

2.2 μ-CT scanning and 3D reconstruction of cancellous bone

The cylindrical specimen of cancellous bone was scanned from one end to another using a μ-CT scanner (SkyScan 1174, Bruker Corporation, Kontich, Belgium) at a voltage of 50 kV and a current of 800 μA, resulting in a scan resolution of 12 μm. A series of images were obtained to illustrate the structure of each cross section of the specimen (Figure 1c & d). The

image stack of 701 images in BMP format was imported into Mimics (Materialise, Leuven, Belgium) for segmentation and creation of the 3D surface geometry. During the segmentation process, the threshold was in the range of -897 ~ -770. The reconstructed 3D digital model of cancellous bone was then imported into Geomagic Wrap (3D Systems Corporation, Rock Hill, South Carolina, USA) to cut a cylindrical 3D model from it. The cylindrical 3D model initially had a diameter of 4 mm and a height of 2.46 mm. It was enlarged to a diameter of 13 mm and a height of 8 mm, which was consistent with the size of the monolithic catalyst in our previous work.[16] After that, the enlarged 3D model was subjected to noise reduction and surface smoothing to obtain an optimized 3D digital model of cancellous bone (marked as BovBone) in stereolithographic (STL) format, which was used in subsequent CFD simulations. For comparison, monolithic catalysts used in our previous work[16] with honeycomb-shaped straight-channel structure (marked as Honeycomb) and tetrahedral periodic structure (marked as Diamond) were also simulated. The morphological parameters of these monolithic catalysts are summarized in Table 1 and their structure are illustrated schematically in Figure 2.

2.3 Computational domain

The computational domain and boundary conditions of monolithic catalysts are shown in Figure 3. To minimize the influence of the boundary conditions, an upstream and a downstream region were generated at the inlet and outlet of the catalyst respectively.[30] The upstream and downstream region were 5 mm and 15 mm in length respectively. They had the same diameter as the catalyst, i.e. 13 mm.

The computational domains were then meshed with the commercial software ANSYS

ICEM CFD (ANSYS Inc., US). Tetrahedral grid was chosen to mesh the computational domains. The generated meshes were imported into ANSYS FLUENT (ANSYS Inc., US) for the subsequent simulations. To verify whether the above grids meet the calculation requirements, mesh independent tests were performed.[31] The elements were 2,056,250, 1,668,097, and 1,255,815 for BovBone-, Honeycomb-, and Diamond-types monolithic catalysts, respectively.

2.4 Governing equations

Full 3D governing equations were applied in all of the simulations to model the behavior of the Newtonian fluids in this study. All simulations were carried out at steady state. Gravitational and external body forces, thermal diffusion, and viscous heating were not taken into consideration in this work.[32] For the laminar flow, a set of equations formulated in Cartesian coordinates with Einstein convention can be written as follows.[33]

Conservation of mass

$$\frac{\partial(\rho u_i)}{\partial x_i}=0 \tag{1}$$

where ρ is density, u_i are the Cartesian components of the velocity vector and x_i are the Cartesian coordinates (i = 1, 2, 3).

Conservation of momentum

$$\frac{\partial}{\partial x_j}(\rho u_i u_j)+\frac{\partial p}{\partial x_i}+\frac{\partial \tau_{ij}}{\partial x_j}=0 \tag{2}$$

where p is pressure, τ_{ij} is the stress tensor and is written as

$$\tau_{ij}=-\mu\left(\frac{\partial u_i}{\partial x_j}+\frac{\partial u_j}{\partial x_i}\right)+\left(\frac{2}{3}\mu\right)\delta_{ij}\frac{\partial u_k}{\partial x_k} \tag{3}$$

where μ is dynamic viscosity and δ_{ij} the Kronecker delta, which is unity for $i = j$, else zero.[33]

Conservation of species i

$$\frac{\partial(\rho u_j Y_i)}{\partial x_j} + \frac{\partial j_{i,j}}{\partial x_j} = 0 \qquad \text{for } i = 1, 2, \ldots, N_g \tag{4}$$

where Y_i is the mass fraction of species i in the mixture, N_g is the number of gas phase species and $j_{i,j}$ is the mass flux of the species i in the direction j calculated as

$$j_{i,j} = -\rho \frac{Y_i}{X_i} D_{i,m} \frac{\partial X_i}{\partial x_j} \tag{5}$$

where X_i represents the molar fraction of species i, $D_{i,m}$ is the diffusion coefficient of species i in the mixture, which is calculated as mass average of the binary diffusion coefficients

$$D_{i,m} = \frac{1 - Y_i}{\sum_{k \neq i}^{N_g} \frac{X_k}{D_{k,i}}} \qquad \text{for } i = 1, 2, \ldots, N_g \tag{6}$$

The binary diffusion coefficient $D_{k,i}$ are calculated using kinetic theory.[34] The molar fraction X_i can be written as

$$X_i = \frac{1}{\sum_{i=1}^{N_g} \frac{Y_i}{M_i}} \frac{Y_i}{M_i} \tag{7}$$

where M_i is the molar weight of species i.

Conservation of energy

$$\frac{\partial(\rho u_j h)}{\partial x_j} - \frac{\partial}{\partial x_j}\left(\lambda \frac{\partial T}{\partial x_j}\right) + \frac{\partial}{\partial x_j} \sum_{i=1}^{N_g} h_i j_{i,j} - u_j \frac{\partial p}{\partial x_j} = 0 \tag{8}$$

where λ is the thermal conductivity of the gas, T is temperature of the gas, h is the enthalpy of the gas and is calculated using the mass average of the enthalpy of each species h_i via

$$h=\sum_{i=1}^{N_g} Y_i h_i \tag{9}$$

where h_i is calculated as

$$h_i=h_i(T_{ref})+\int_{T_{ref}}^{T} c_{p,i}\,dT \tag{10}$$

where T_{ref} is reference temperature (298 K). The specific heat capacity at constant pressure of each species $c_{p,i}$ is computed from piecewise-polynomial functions.[31] Additionally, viscosity, thermal conductivity, and the specific heat of the gas mixture are calculated via mixing-law, which depends on the local composition and temperature.[35]

The density of the gas mixture ρ is computed using the ideal gas law to close the governing equations:

$$p=\frac{\rho RT}{\sum_{i=1}^{N_g} X_i M_i} \tag{11}$$

where R is universal gas constant (8.314 $J\cdot mol^{-1}\cdot K^{-1}$).

All the governing equations are solved with the finite-volume commercial software ANSYS FLUENT.[36] A second order upwind scheme was applied for the calculation of flow and energy.[37] The coupled scheme was applied for the pressure-velocity coupling. The simulations were considered complete when the absolute value of residuals for continuity, energy and the momentum equation all falls below 10^{-4}.

2.5 Reaction kinetics model

Methanation reaction from syngas to SNG is accompanied by several side reactions, and the most dominant reaction is[38]

$$CO + 3H_2 = CH_4 + H_2O \quad \Delta H_{298K} = -206.28\, KJ \cdot mol^{-1} \tag{12}$$

For the sake of simplicity, only the aforementioned dominant reaction was taken into consideration, reaction kinetics of which has been investigated in detail by Kopyscinski et al.[38]

$$r = \frac{k \cdot K_C \cdot p_{CO}^{0.5} \cdot p_{H_2}^{0.5}}{¿¿} \tag{13}$$

where r is reaction rate of syngas methanation, k is reaction rate constant, K is adsorption constant. The determination of reaction kinetics was carried out over Ni/Al_2O_3-type catalyst, which was consistent with the catalyst used in our previous experiments.[16] In addition, the reaction of syngas methanation was performed at temperature ranging from 553 to 633 K, which were close to the temperature of our previous work (648 K).[16] Thus the reaction kinetics, i.e. Eq. (13) was adopted to simulate syngas methanation in this work.

To describe the diffusion in catalysts, we adopted a pseudo-phase approach by employing effective transport coefficients.[35] The effective transport coefficient depends mainly on the diffusion resistance within the porous washcoat, and can be expressed by the effectiveness factor η

$$\eta = \tanh \frac{(¿\phi)}{\phi} ¿ \tag{14}$$

where Φ represents the Thiele modulus.[39,40] For a first order reaction, the Thiele modulus is calculated as

$$\phi = R\sqrt{\frac{k}{D_{eff}}} \tag{15}$$

where R is the geometric size defined as the volume divided by the surface area of the

catalyst, k is the reaction rate constant and D_{eff} is the effective diffusion coefficient in the washcoat.[41]

The chemical reactions at the surface of catalyst are coupled with the species fields via boundary conditions in Eq. (5).[33] Under steady-state conditions, the diffusion mass flux of species i at the interface of gas and washcoat must equal to the consumption or production rate of such species[31]

$$\vec{n} \cdot \vec{j}_i = R_i^{het} = \eta F_{cat/geo} M_i \dot{s}_i \tag{16}$$

where $\vec{n}$ is the outward-pointing unit vector normal to the surface, $\vec{j}_i$ is the diffusion mass flux in Eq. (6), R_i^{het} is the reaction rate expressed in terms of the mass fraction of species i at the catalytic surface, $\dot{s}_i$ is the molar net consumption/production rate of species i and $F_{cat/geo}$ is the ratio of active Ni surface area A_{cat} to the geometric surface area A_{geo} of the catalyst

$$F_{cat/geo} = A_{cat} / A_{geo} \tag{17}$$

The parameter $F_{cat/geo}$ was determined experimentally by using CO temperature-programmed desorption, as reported by Boll et al.[42] The $F_{cat/geo}$ = 0.18 was used to mimic the 3D-printed monolithic catalysts used in our previous work.[16]

2.6 Boundary conditions

The boundary conditions were set as closely as possible to the experimental conditions in our previous work[16] to facilitate a direct comparison between numerical and experimental results. The composition of syngas at the inlet was H_2:CO:N_2 = 3:1:1 (molar fraction), with gas flow velocities ranging from 0.00444 to 0.0533 m/s. Due to the relatively slow flow

velocities, small Reynolds number (ℜ¿10) were obtained, indicating a laminar flow. At the outlet of the computational domain, an outlet pressure condition p_{out} =1 atm was used. In addition, no-slip boundary conditions were set at the walls, and the species were set to have no diffusive flux at the walls.

Heat transfer between the catalysts and the fluid was carried out by forced convection. The heat transfer coefficient was set to 70 $W \cdot m^{-2} \cdot K^{-1}$, which was a typical value for forced convection heat transfer.[43] The temperatures at inlet and outlet of the computational domains as well as the temperature of the wall which was not involved in the reaction were set to 648 K. The discrete ordinates model was applied to simulate the thermal radiation on the catalyst surface. The emissivity value in the simulations was assumed to be constant at a value of 0.9. This assumption simplifies the fact that the emissivity is dependent on the surface condition and wavelength.[33,44]

4. RESULTS AND DISCUSSION

4.1 Model validation

Simulations of methanation from syngas to SNG were carried out over the 3D-printed monolithic catalysts and the results were compared with experimental ones reported in our previous work.[16] As shown in Table 2, the difference between the simulation and experimental results of honeycomb-type monolithic catalyst is small in terms of temperature difference between the inlet and outlet of the catalysts. For diamond-type monolithic catalyst, however, the simulation results deviate slightly from the experimental results. In terms of the conversion of CO, the simulation results are found to be in good agreement with the experimental ones for both monolithic catalysts with periodic structure. Take both the

temperature difference and conversion of CO into consideration, the simulation results are in line with the experimental results, indicating that the simulation is reasonable.

4.2 Velocity profiles within 3D-printed monolithic catalysts

The flow fields of gas across three monolithic catalysts are shown in Figure 4. For honeycomb-type monolithic catalyst, the flow field is very homogeneous due to the uniform distribution of the straight channels. Similar to that of honeycomb-type monolithic catalyst, the gas flow within diamond-type one is also homogenous due to its regular structure. However, the gas velocity within diamond-type monolithic catalyst is much higher when compared to honeycomb-type one. One of the reasons is that the temperature of gas inside diamond-type monolithic catalyst is greater than honeycomb-type one, which will be discussed later. The difference in porosity is another reason for the large difference in velocity profiles.

The gas velocity along the axial direction tends to increase first and then decrease within the two monolithic catalyst with periodic structure. The reason is that the temperature rises gradually as the reaction proceeds at the inlet, causing the flow velocity to increase. Since syngas methanation is a reaction in which the total volume decreases, the flow velocity will decrease as a result of reaction, which indicates that the flow velocity has a strong interaction with the chemical reaction and the temperature distribution.

Compared to monolithic catalyst with periodic structure, the gas flow is very inhomogeneous within bio-inspired monolithic catalyst due to the irregularity of its structure. The gas velocity in some regions is higher than that in monolithic catalyst with periodic structure. While in other regions the gas velocity is very low and led to stagnation, which is

rarely seen in the case of monolithic catalyst with periodic structure. As can be seen from Figure 4, the bio-inspired monolithic catalyst shows strong vortexes no matter it is inside the catalyst or at the inlet and outlet. The vortex within bio-inspired monolithic catalyst might intensify the radial mixing of reactants, resulting in more complete reaction.

4.3 Temperature profiles

The temperature fields within three monolithic catalysts are shown in Figure 5. For bio-inspired monolithic catalyst, the temperature within the catalyst is uneven. While for monolithic catalysts with periodic structure, i.e., honeycomb-type and diamond-type monolithic catalysts, the temperatures are homogeneous just like their velocity profiles.

Figure 6 shows the axial area-averaged temperature profiles of the gas phase in the three monolithic catalysts obtained by simulations. As mentioned above, methanation of syngas releases a lot of heat, so the temperature of the gas phase rises rapidly during the reaction. Before entering the catalyst ($z < 5$ mm), the temperature of the gas phase increases slightly due to the thermal radiation of the reaction region. When the gas gets contact with the catalyst, temperature rises abruptly and reaches a maximum at about $z \approx 7$ mm. The reason for fast increase in temperature is that the concentration of the reactants is high at the inlet, resulting in a high rate of reaction, which in turn further accelerates the progress of reaction. Subsequently, as the reactants are consumed, the reaction rate gradually decreases. Due to the heat exchange between the gas phase and external environment, the temperature of the gas phase decreased gradually.

Comparison among the three monolithic catalysts found that the temperature of the gas phase within diamond-type monolithic catalyst is the highest, while the temperature of the

gas phase within honeycomb-type monolithic catalyst is the lowest. The channels of honeycomb-type monolithic catalyst are straight, it is easier for the gas to carry the heat released by the reaction out, so the temperature within is the lowest. While the channels of diamond-type and bio-inspired monolithic catalysts are tortuous, the mixing of the reactants and the contact of them with the catalysts are more sufficient. As a result, the methanation of syngas within these monolithic catalysts are more thorough and releases more heat. Due to the excellent heat transfer performance of the bio-inspired monolithic catalyst, it is easier to transfer heat away when compared with diamond-type one. For exothermic reactions, poor heat transfer might lead to the formation of hot-spots, causing catalyst deactivation. Therefore, bio-inspired monolithic catalyst is preferable in terms of heat transfer.

4.4 Concentration profiles

Figure 7 shows the concentration fields of CO, H_2, and CH_4 in the three types of monolithic catalyst. For monolithic catalysts with periodic structures, the concentration profiles of reactants within the catalysts are very smooth, but this is not the case for bio-inspired monolithic catalyst, which again validates the irregularity of its structure.

Figure 8 shows the corresponding axial area-averaged molar fraction of CO, H_2, and CH_4. The concentration of reactants decreases even before the gas get contact with catalyst ($z < 5$ mm) due to molecular diffusion. During the methanation reaction, the reactants within the catalyst are consumed rapidly, resulting in a large concentration difference at both sides of the catalyst, which allows the reactants enter the catalyst by molecular diffusion. This is also the reason why the concentration of the product increases before entering the catalyst. It is worth noting that after the gas flows out of the catalyst ($z > 13$ mm), the concentration of the

various substances in monolithic catalysts with periodic structures are substantially constant. While in bio-inspired monolithic catalyst, the concentration of H_2 and CH_4 changes slightly. As mentioned above, due to the structural irregularities of bio-inspired monolithic catalyst, the velocity, temperature, and concentration fields in the downstream region are inhomogeneous, resulting in changes in their concentration even after H_2 and CH_4 leave the catalytic region. The vortex at the outlet of bio-inspired monolithic catalyst is also the cause of the change in the concentration of H_2 and CH_4.

By comparing the conversion of CO over the three different monolithic catalysts, it is found that the conversion of CO over diamond-type monolithic catalyst is the highest (88%), followed by the one over bio-inspired monolithic catalyst (82%). The conversion of CO over honeycomb-type monolithic catalyst is only 58%. As shown in Table 1, the porosity of the monolithic catalyst varies greatly. In order to eliminate the influence of porosity on the reaction, the ability of the catalysts to convert CO per unit time and mass is also determined. In the case of same mass of catalyst, the amount of CO converted over bio-inspired monolithic catalyst is about 30% more than that converted over diamond-type one, which is about twice of that over honeycomb-type one. The result indicates that bio-inspired monolithic is more conducive for the reaction to proceed.

4.5 Influence of the inlet velocity on methanation of syngas

In order to explore the influence of inlet gas velocity, the methanation reaction of syngas is further simulated at five different velocities. Figure 9 shows the temperature difference between the inlet and outlet of the monolithic catalysts and the maximum temperature of the gas phase as functions of the inlet gas velocity. For honeycomb-type and bio-inspired

monolithic catalysts, the temperature difference decreases as the inlet velocity increases. This is because when the inlet gas velocity is low, the reaction proceeds more thoroughly. Therefore, the reactants are completely consumed at the inlet of the catalysts and a large amount of released heat accumulates, resulting in a large temperature difference between the inlet and outlet of the catalysts. As the inlet gas velocity increases, the reaction occurs throughout the catalysts, allowing the released heat to distribute along the catalyst, resulting in lower temperature difference between inlet and outlet of the catalyst. For diamond-type monolithic catalyst, the temperature difference exhibits a similar trend at inlet gas velocities above 0.0178 m/s. However, when the inlet velocities are below 0.0178 m/s, the temperature difference is observed to increase as the inlet gas velocity increases. This is attributed to the high conversion of CO over diamond-type monolithic catalyst as discussed in Section 4.4.

In contrast to the trend of the temperature difference across the three monolithic catalysts, the maximum temperature of the gas phase increases with increasing inlet gas velocity. This can be explained by a positive correlation between the reaction rate and the concentration of reactants. Moreover, the maximum temperature in diamond-type monolithic catalyst increases much higher at same inlet velocity when compared with other types of monolithic catalysts, which further demonstrates that diamond-type monolithic catalyst is not conducive to heat transfer.

4.6 Comparison among different monolithic catalyst in terms of catalytic performance

Figure 10a plots the conversion of CO as a function of the inlet gas velocity over different monolithic catalysts. At an inlet gas velocity of 0.00444 m/s, the conversion of CO over the three monolithic catalysts are all close to 100%. As the inlet velocity gas increases,

the conversion of CO decreases to various degrees, among which honeycomb-type monolithic catalyst decreases the most. As the inlet gas velocity increases, the contact of reactants with the active sites of the catalysts decreases, which leads to the reactants flow out before conversion to CH_4. Honeycomb-type monolithic catalyst has a straight-channel structure, the reactants flow more easily. While the tortuous channels of diamond-type and bio-inspired monolithic catalysts allow the reactants to contact with active sites more frequently. Thus, the conversion of CO over diamond-type and bio-inspired monolithic catalysts decrease less when the inlet gas velocity increases.

In chemical industry, the catalytic capacity per unit mass of catalyst is a key factor to evaluate the performance of catalysts. As shown in Figure 10b, with increasing the inlet gas velocity, the amount of CO that can be catalytically converted per unit mass increased gradually. Bio-inspired monolithic catalyst shows higher capacity than monolithic catalysts with periodic structures at the same catalyst mass, further verifying that the cancellous bone is advantageous as a structure of monolithic catalysts.

To further interpret the superior catalytic activity of bio-inspired monolithic catalyst, the velocity, temperature, and concentration fields on cross sections of different positions on the catalyst are investigated. As shown in Figure 11, gas flow exists at different positions in bio-inspired monolithic catalyst, which proves the superior connectivity of the structure of cancellous bone. In addition, large vortexes appear at different positions in bio-inspired monolithic catalyst, and the temperature of gas phase and concentration of CO both have large differences even at the same axial position, which is rarely observed in the catalyst with periodic structure. The existence of vortices can aggravate the mixing between different

species and increase the residence time of the reactants, so that they can be converted more effectively.[45]

5. CONCLUSIONS

In this contribution, methanation reaction from syngas to SNG over 3D-printed monolithic catalyst was simulated using CFD. The deviation of simulation results from experimental ones is within 15%, suggesting that the models employed in simulation are reasonable. The results show that the ability of bio-inspired monolithic catalyst to convert syngas into SNG is superior when compared with that of monolithic catalyst with periodic structure. Turbulent flow resulted from the irregular structure of bio-inspired monolithic catalyst affects the transport scheme of mass flow, diffusion and temperature, which should be responsible for the promoted catalytic performance.

NOMENCLATURE

Latin letters

A	surface area, m^2
c_p	specific heat capacity, $J \cdot kg^{-1} \cdot K^{-1}$
$D_{i,m}$	diffusion coefficient of species i in the mixture, $m \cdot s^{-2}$
$D_{k,i}$	binary diffusion coefficient, $m \cdot s^{-2}$
D_{eff}	effective diffusion coefficient, $m^2 \cdot s^{-1}$
$F_{\text{cat/geo}}$	ratio of catalytic active area to geometric area, dimensionless
g	gravity acceleration, $m \cdot s^{-2}$
h	specific enthalpy, $J \cdot kg^{-1}$

ΔH	Gibbs free energy, $kJ \cdot mol^{-1}$
$j_{i,j}$	mass flux of species i in the direction j, $kg \cdot m^{-2} \cdot s^{-1}$
$\vec{j}_i$	diffusion mass flux, $kg \cdot m^{-2} \cdot s^{-1}$
k	reaction rate constant, $mol \cdot kg_{cat}^{-1} \cdot s^{-1}$
K	adsorption constant
M_i	molar weight of species i, $kg \cdot mol^{-1}$
N_g	number of gas phase species, dimensionless
p	pressure, Pa or atm
r	reaction rate of syngas methanation, $mol \cdot kg_{cat}^{-1} \cdot s^{-1}$
Re	Reynolds number, dimensionless
R	ratio of catalyst volume to surface area, m; universal gas constant, $8.314\ J \cdot mol^{-1} \cdot K^{-1}$
R_i^{het}	production rate of species i, $kg \cdot m^{-3} \cdot s^{-1}$
$\dot{s}_i$	molar net consumption/production rate of species i, $mol \cdot m^{-2} \cdot s^{-1}$
T	temperature, K
T_{ref}	reference temperature, taken to be 298 K
u_i	velocity components, $m \cdot s^{-1}$
x_i	coordinate in i direction, m
X_i	molar fraction of species i, dimensionless
Y_i	mass fraction of the species i, dimensionless

Greek letters

ρ	density, $kg \cdot m^{-3}$
τ	stress tensor, N
μ	dynamic viscosity, $Pa \cdot s$
δ_{ij}	Kronecker delta, dimensionless

λ thermal conductivity, $W \cdot m^{-1} \cdot k^{-1}$

η effectiveness factor, dimensionless

Φ Thiele modulus, dimensionless

Abbreviations

CFD computational fluid dynamics

CT computer tomography

ACKNOWLEDGMENTS

The work was supported financially by National Natural Science Foundation of China (21606185, 21673187) and Fundamental Research Funds for the Central Universities (20720190038).

REFERENCES

1. Lefevere J, Mullens S, Meynen V. The impact of formulation and 3D-printing on the catalytic properties of ZSM-5 zeolite. *Chem. Eng. J.* 2018;349:260-268.

2. Couck S, Lefevere J, Mullens S, et al. CO_2 , CH_4 and N_2 separation with a 3DFD-printed ZSM-5 monolith. *Chem. Eng. J.* 2017;308:719-726.

3. Thakkar H, Eastman S, Al-Naddaf Q, Rownaghi AA, Rezaei F. 3D-printed metal-organic framework monoliths for gas adsorption processes. *ACS Appl. Mater. Interfaces.* 2017;9(41):35908-35916.

4. Guettel R, Turek T. Assessment of micro-structured fixed-bed reactors for highly exothermic gas-phase reactions. *Chem. Eng. Sci.* 2010;65(5):1644-1654.

5. Avila P, Montes M, Miró EE. Monolithic reactors for environmental applications. *Chem. Eng. J.* 2005;109(1-3):11-36.

6. Thakkar H, Eastman S, Hajari A, Rownaghi AA, Knox JC, Rezaei F. 3D-printed zeolite monoliths for CO_2 removal from enclosed environments. *ACS Appl Mater Interfaces*. 2016;8(41):27753-27761.

7. Stuecker JN, Miller JE, Ferrizz RE, Mudd JE, Cesarano J. Advanced support structures for enhanced catalytic activity. *Ind. Eng. Chem. Res.* 2004;43(1):51-55.

8. Patcas FC, Garrido GI, Kraushaar-Czarnetzki B. CO oxidation over structured carriers: A comparison of ceramic foams, honeycombs and beads. *Chem. Eng. Sci.* 2007;62(15):3984-3990.

9. Parra-Cabrera C, Achille C, Kuhn S, Ameloot R. 3D printing in chemical engineering and catalytic technology: structured catalysts, mixers and reactors. *Chem. Soc. Rev.* 2018;47(1):209-230.

10. Zhu C, Qi Z, Beck VA, et al. Toward digitally controlled catalyst architectures: Hierarchical nanoporous gold via 3D printing. *Sci. Adv.* 2018;4(8):eaas9459.

11. Manzano JS, Weinstein ZB, Sadow AD, Slowing II. Direct 3D printing of catalytically active structures. *ACS Catal.* 2017;7(11):7567-7577.

12. Zhou X, Liu C. Three-dimensional printing of porous carbon structures with tailorable pore sizes. *Catal. Today.* 2018;347:2-9.

13. Parlett CM, Wilson K, Lee AF. Hierarchical porous materials: Catalytic applications. *Chem. Soc. Rev.* 2013;42(9):3876-3893.

14. Díaz-Marta AS, Tubío CR, Carbajales C, et al. Three-dimensional printing in catalysis: Combining 3D heterogeneous copper and palladium catalysts for multicatalytic multicomponent reactions. *ACS Catal.* 2017;8(1):392-404.

15. Zhou X, Liu C-j. Three-dimensional printing for catalytic applications: Current status

and perspectives. *Adv. Funct. Mater.* 2017;27(30).

16. Li Y, Chen S, Cai X, et al. Rational design and preparation of hierarchical monoliths through 3D printing for syngas methanation. *J. Mater. Chem. A* 2018;6(14):5695-5702.

17. Quintanilla A, Casas JA, Miranzo P, Osendi MI, Belmonte M. 3D-Printed Fe-doped silicon carbide monolithic catalysts for wet peroxide oxidation processes. *Appl. Catal., B* 2018;235:246-255.

18. Li X, Rezaei F, Rownaghi AA. Methanol-to-olefin conversion on 3D-printed ZSM-5 monolith catalysts: Effects of metal doping, mesoporosity and acid strength. *Microporous Mesoporous Mater.* 2019;276:1-12.

19. Azuaje J, Tubío CR, Escalante L, et al. An efficient and recyclable 3D printed α-Al_2O_3 catalyst for the multicomponent assembly of bioactive heterocycles. *Appl. Catal., A* 2017;530:203-210.

20. Bauer J, Hengsbach S, Tesari I, Schwaiger R, Kraft O. High-strength cellular ceramic composites with 3D microarchitecture. *Proc Natl Acad Sci USA.* 2014;111(7):2453-2458.

21. Gantenbein S, Masania K, Woigk W, Sesseg JPW, Tervoort TA, Studart AR. Three-dimensional printing of hierarchical liquid-crystal-polymer structures. *Nature* 2018;561(7722):226-230.

22. Wegst UG, Bai H, Saiz E, Tomsia AP, Ritchie RO. Bioinspired structural materials. *Nat Mater.* 2015;14(1):23-36.

23. Coppens M-O. A nature-inspired approach to reactor and catalysis engineering. *Curr.*

Opin. Chem. Eng. 2012;1(3):281-289.

24. Martin JJ, Fiore BE, Erb RM. Designing bioinspired composite reinforcement architectures via 3D magnetic printing. *Nat Commun.* 2015;6:8641.

25. Trogadas P, Nigra MM, Coppens M-O. Nature-inspired optimization of hierarchical porous media for catalytic and separation processes. *New J. Chem.* 2016;40(5):4016-4026.

26. Compton BG, Lewis JA. 3D-printing of lightweight cellular composites. *Adv. Mater.* 2014;26(34):5930-5935.

27. Studart AR. Additive manufacturing of biologically-inspired materials. *Chem. Soc. Rev.* 2016;45(2):359-376.

28. Dhondt S, Vanhaeren H, Van Loo D, Cnudde V, Inze D. Plant structure visualization by high-resolution X-ray computed tomography. *Trends Plant Sci.* 2010;15(8):419-422.

29. Dixon PG, Muth JT, Xiao X, Skylar-Scott MA, Lewis JA, Gibson LJ. 3D printed structures for modeling the Young's modulus of bamboo parenchyma. *Acta Biomater.* 2018;68:90-98.

30. Wehinger GD, Eppinger T, Kraume M. Detailed numerical simulations of catalytic fixed-bed reactors: Heterogeneous dry reforming of methane. *Chem. Eng. Sci.* 2015;122:197-209.

31. Dong Y, Korup O, Gerdts J, Roldán Cuenya B, Horn R. Microtomography-based CFD modeling of a fixed-bed reactor with an open-cell foam monolith and experimental verification by reactor profile measurements. *Chem. Eng. J.* 2018;353:176-188.

32. Quiceno R, Pérez-Ramírez J, Warnatz J, Deutschmann O. Modeling the high-

temperature catalytic partial oxidation of methane over platinum gauze: Detailed gas-phase and surface chemistries coupled with 3D flow field simulations. *Appl. Catal., A* 2006;303(2):166-176.

33. Wehinger GD, Kraume M, Berg V, et al. Investigating dry reforming of methane with spatial reactor profiles and particle-resolved CFD simulations. *AIChE J.* 2016;62(12):4436-4452.

34. Benzinger W, Daymo E, Hettel M, et al. Reverse water gas shift (RWGS) over Ni–Spatially-resolved measurements and simulations. *Chem. Eng. J.* 2019;362:430-441.

35. Maffei T, Gentile G, Rebughini S, et al. A multiregion operator-splitting CFD approach for coupling microkinetic modeling with internal porous transport in heterogeneous catalytic reactors. *Chem. Eng. J.* 2016;283:1392-1404.

36. Diani A, Bodla KK, Rossetto L, Garimella SV. Numerical investigation of pressure drop and heat transfer through reconstructed metal foams and comparison against experiments. *Int. J. Heat Mass Transfer.* 2015;88:508-515.

37. Bianchi E, Groppi G, Schwieger W, Tronconi E, Freund H. Numerical simulation of heat transfer in the near-wall region of tubular reactors packed with metal open-cell foams. *Chem. Eng. J.* 2015;264:268-279.

38. Kopyscinski J, Schildhauer TJ, Vogel F, Biollaz SMA, Wokaun A. Applying spatially resolved concentration and temperature measurements in a catalytic plate reactor for the kinetic study of CO methanation. *J. Catal.* 2010;271(2):262-279.

39. Hayes RE, Fadic A, Mmbaga J, Najafi A. CFD modelling of the automotive catalytic converter. *Catal. Today.* 2012;188(1):94-105.

40. Chan D, Tischer S, Heck J, Diehm C, Deutschmann O. Correlation between catalytic activity and catalytic surface area of a Pt/Al_2O_3 DOC: An experimental and microkinetic modeling study. *Appl. Catal., B* 2014;156-157:153-165.

41. Weisz PB. Diffusion and chemical transformation. *Science* 1973;179(4072):433-440.

42. Boll W, Tischer S, Deutschmann O. Loading and aging effects in exhaust gas after-treatment catalysts with Pt as active component. *Ind. Eng. Chem. Res.* 2010;49(21):10303-10310.

43. Wen D, Ngoc Cong T, He Y, Chen H, Ding Y. Heat transfer of gas-solid two-phase mixtures flowing through a packed bed. *Chem. Eng. Sci.* 2007;62(16):4241-4249.

44. Hettel M, Diehm C, Bonart H, Deutschmann O. Numerical simulation of a structured catalytic methane reformer by DUO: The new computational interface for OpenFOAM® and DETCHEM™. *Catal. Today.* 2015;258:230-240.

45. Cao Z, Li T, Zhang Q, Zhou H, Song C, You F. Systems modeling, simulation and analysis for robust operations and improved design of entrained-flow pulverized coal gasifiers. *Energy* 2018;148:941-964.

Figure captions

FIGURE 1. Side (a) and top (b) views of the cancellous bone specimen from bovine humerus; (c) and (d) are two typical images of the cross section of the specimen obtained by μ-CT scanning.

FIGURE 2. 3D digital models simulated (top), 3D-printed monolithic catalysts (middle), and their corresponding cross sections (bottom).

FIGURE 3. Sketch of the computational domain and boundary conditions for CFD simulations of methanation from syngas to SNG.

FIGURE 4. The simulated flow fields (top) and velocity vectors (bottom) in three monolithic catalysts at inlet gas velocity of 0.0533 m/s.

FIGURE 5. The simulated temperature fields in three monolithic catalysts at inlet velocity of 0.0533 m/s.

FIGURE 6. The axial area-averaged temperature profiles of the three monolithic catalysts at inlet gas velocity of 0.0533 m/s.

FIGURE 7. The simulated concentration fields of CO (top), H_2 (middle) and CH_4 (bottom) in three monolithic catalysts at inlet air velocity of 0.0533 m/s.

FIGURE 8. The concentration profiles of CO, H_2 and CH_4 along the axial coordinate of the three monolithic catalysts at inlet gas velocity of 0.0533 m/s.

FIGURE 9. Temperature difference between the inlet and outlet of monolithic catalysts as well as the maximum temperature within the catalysts against the inlet gas velocity.

FIGURE 10. Conversion (a) and consumption rate of CO (b) against the inlet gas velocity over different monolithic catalysts.

FIGURE 11. Translational cut plane plots of the velocity vector (top), temperature (middle) and mass fraction of CO (bottom) through bio-inspired monolithic catalyst at inlet gas velocity of 0.0533 m/s.

Table captions

Table 1. Morphological parameters of 3D-printed monolithic catalysts

Table 2. Comparison between experimental and simulation results in terms of the temperature difference and CO conversion over monolithic catalysts with periodic structure at an inlet gas velocity of 0.0533 m/s.

FIGURE 1

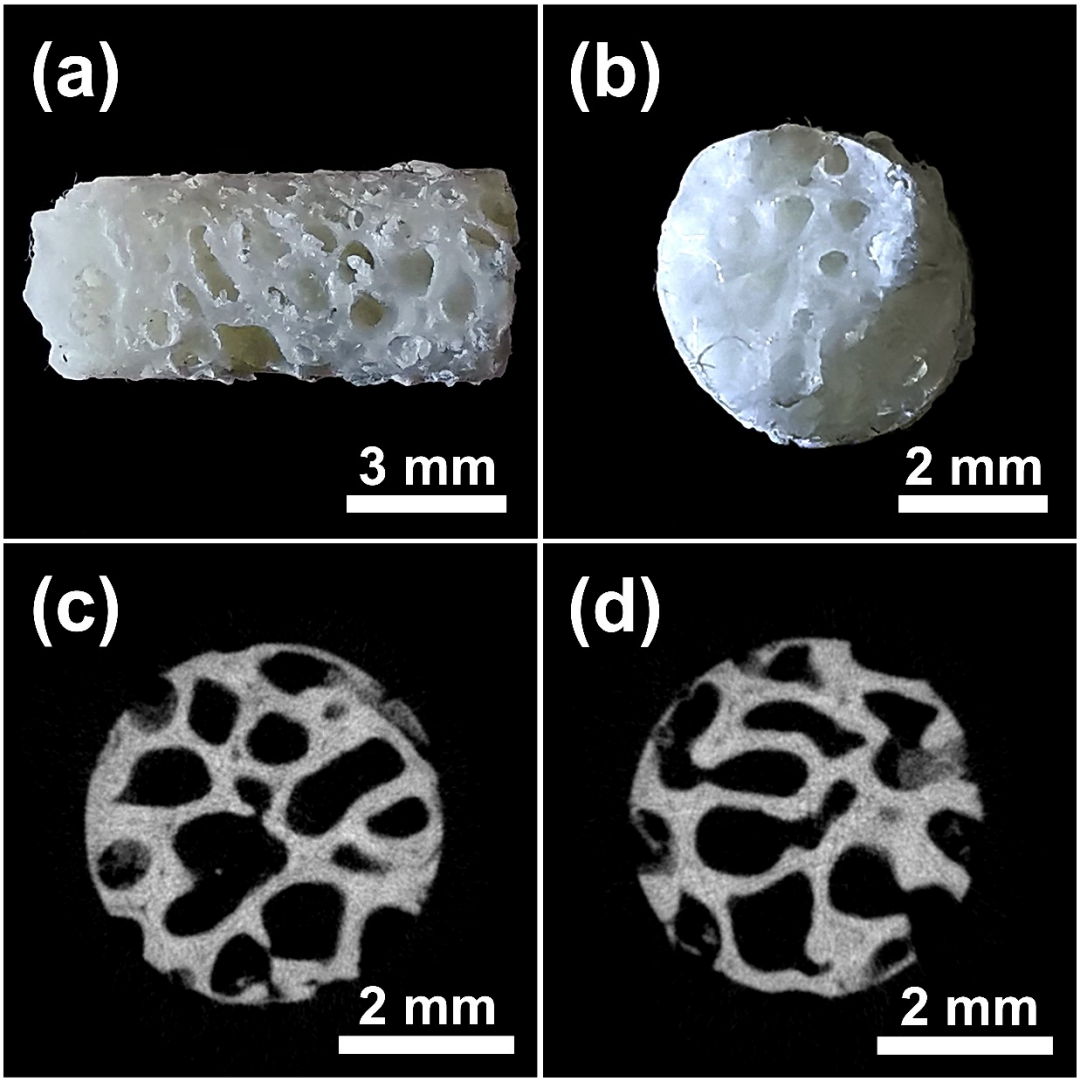

FIGURE 2

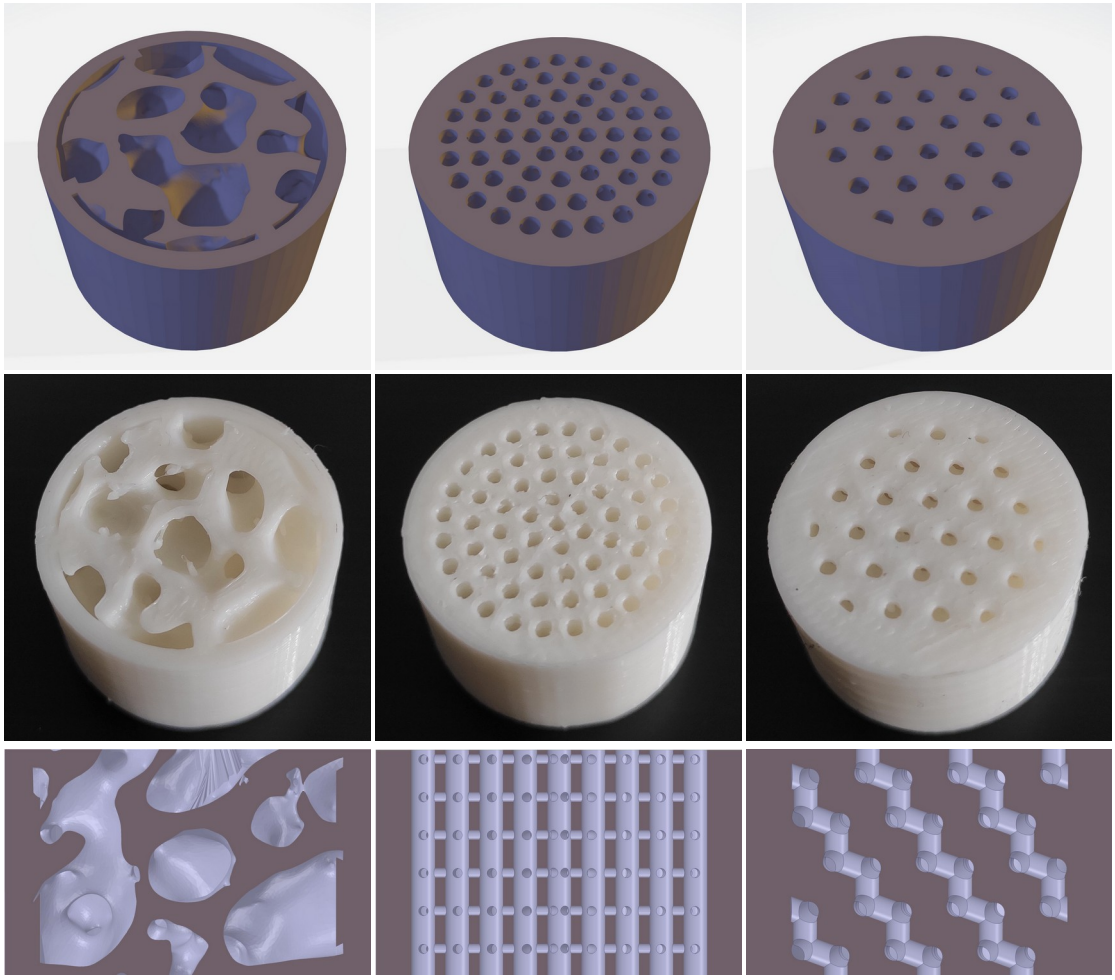

FIGURE 3

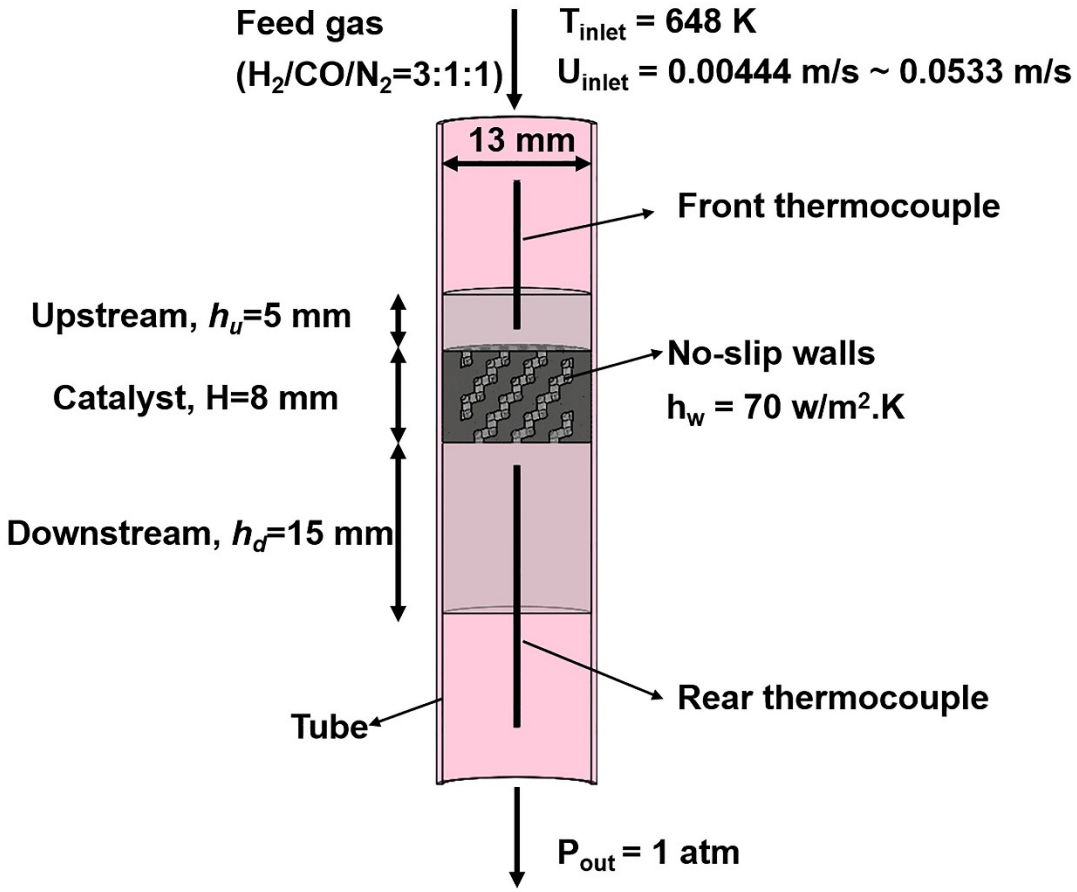
Feed gas
(H2/CO/N2=3:1:1)
Tinlet = 648 K
Uinlet = 0.00444 m/s ~ 0.0533 m/s
13 mm
Front thermocouple
Upstream, hu=5 mm
Catalyst, H=8 mm
No-slip walls
hw = 70 w/m2.K
Downstream, hd=15 mm
Rear thermocouple
Tube
Pout = 1 atm

FIGURE 4

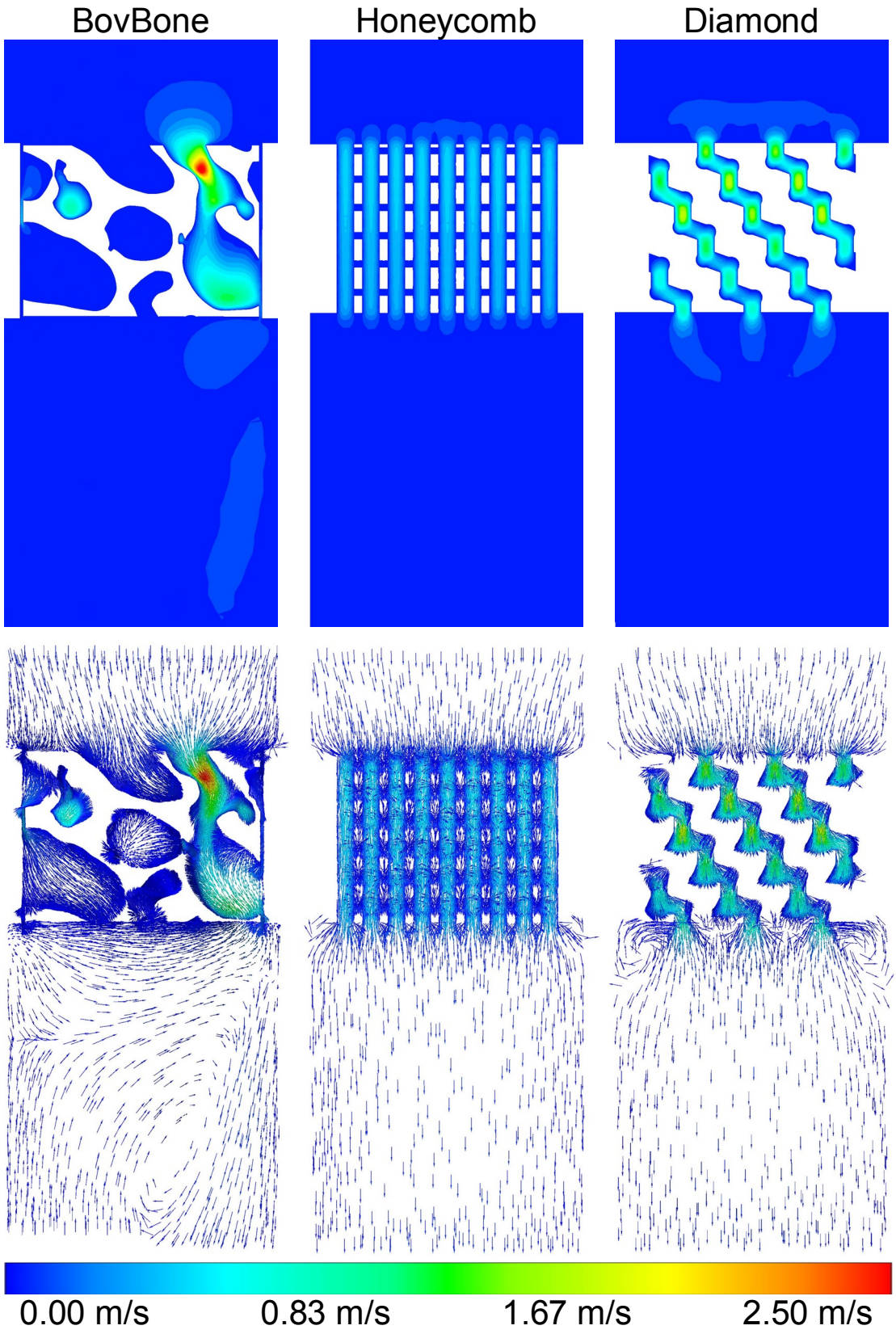

FIGURE 5

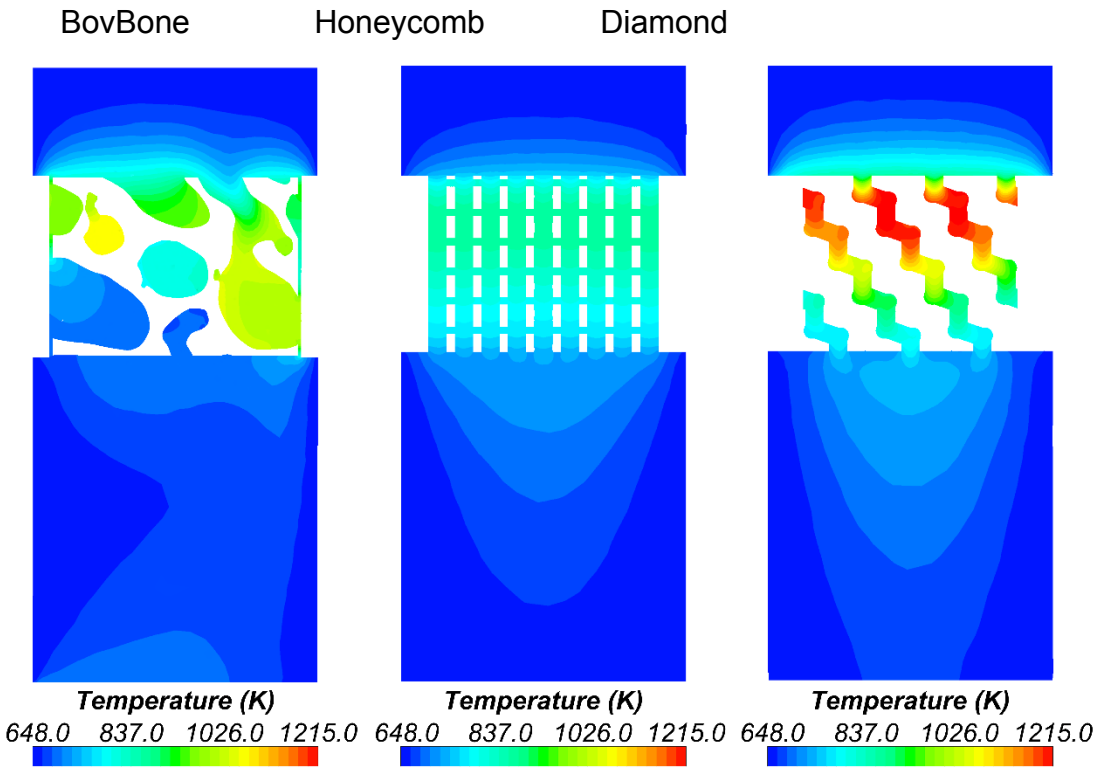
BovBone
Honeycomb
Diamond
Temperature (K)
648.0 837.0 1026.0 1215.0
Temperature (K)
648.0 837.0 1026.0 1215.0
Temperature (K)
648.0 837.0 1026.0 1215.0

FIGURE 6

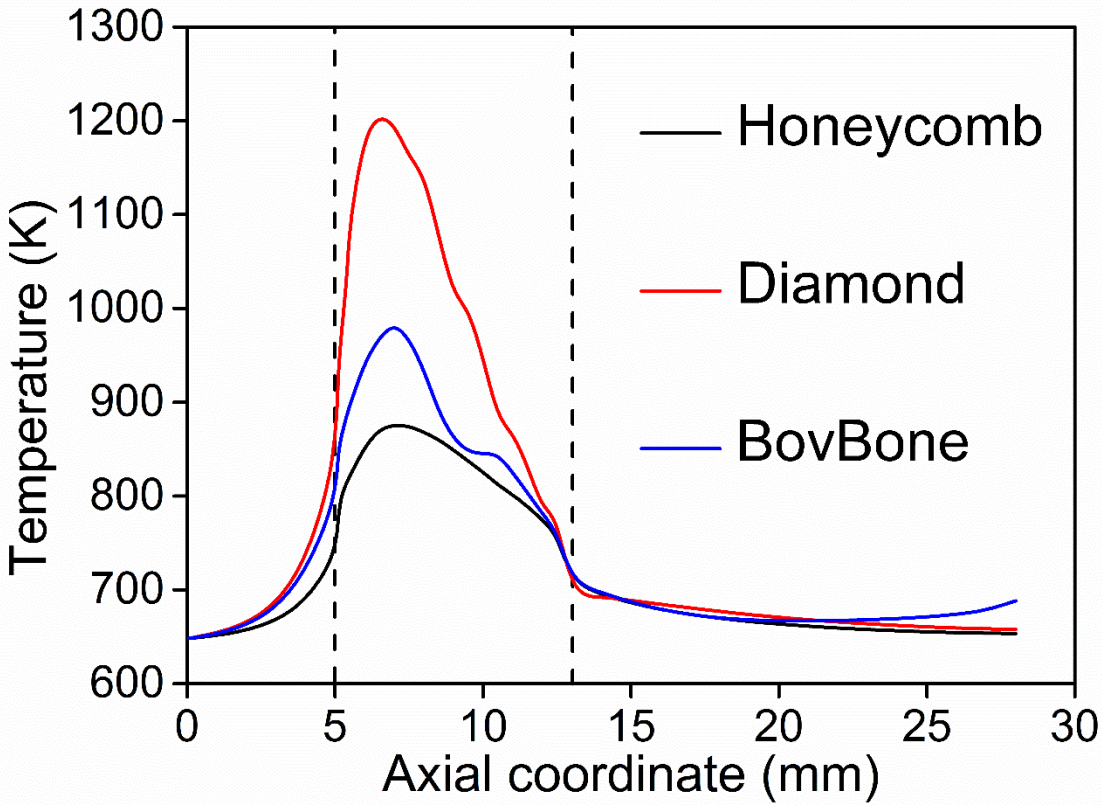
Temperature (K)
1300
1200
1100
1000
900
800
700
600
0
5
10
15
20
25
30
Axial coordinate (mm)
Honeycomb
Diamond
BovBone

FIGURE 7

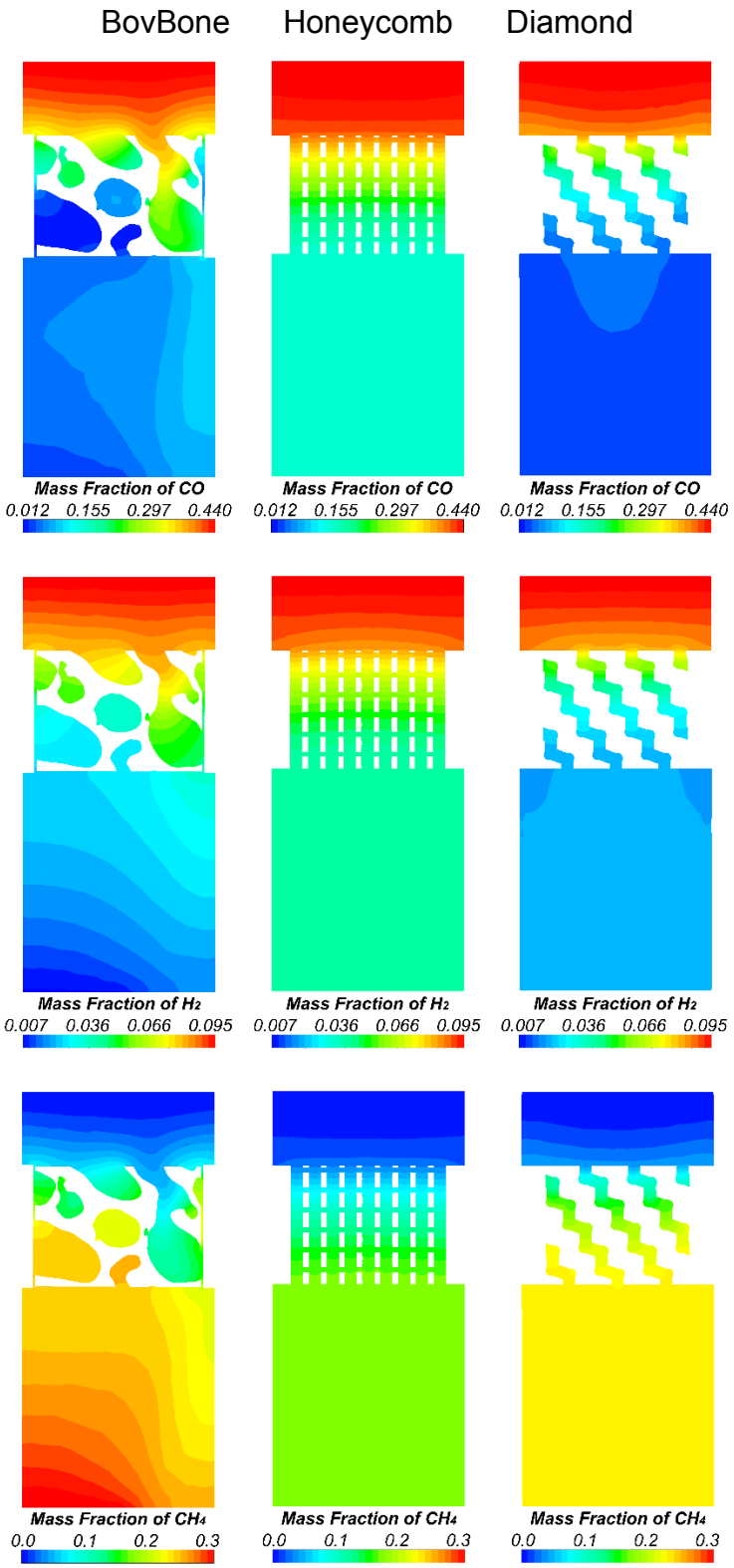
BovBone
Honeycomb
Diamond
Mass Fraction of CO
0.012 0.155 0.297 0.440
Mass Fraction of H2
0.007 0.036 0.066 0.095
Mass Fraction of CH4
0.0 0.1 0.2 0.3

FIGURE 8

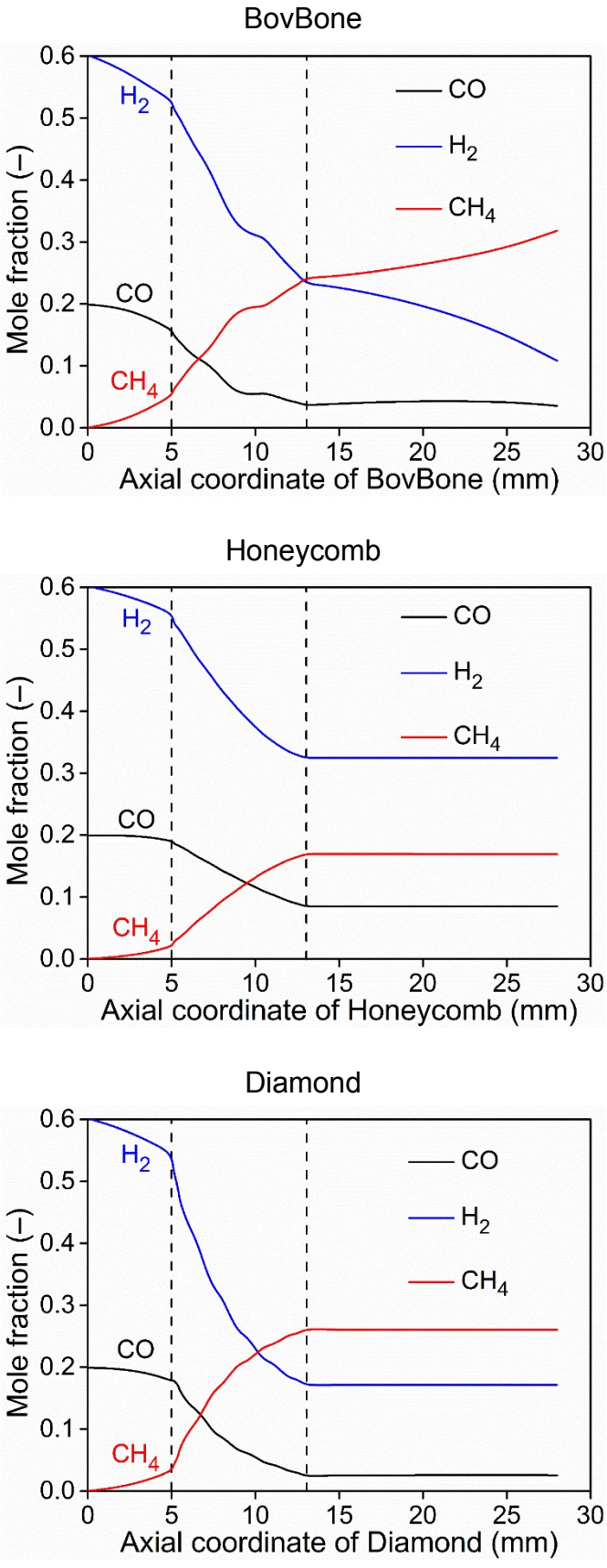
BovBone
Mole fraction (–)
Axial coordinate of BovBone (mm)
Honeycomb
Axial coordinate of Honeycomb (mm)
Diamond
Axial coordinate of Diamond (mm)
CO
H2
CH4
0.0
0.1
0.2
0.3
0.4
0.5
0.6
0
5
10
15
20
25
30

FIGURE 9

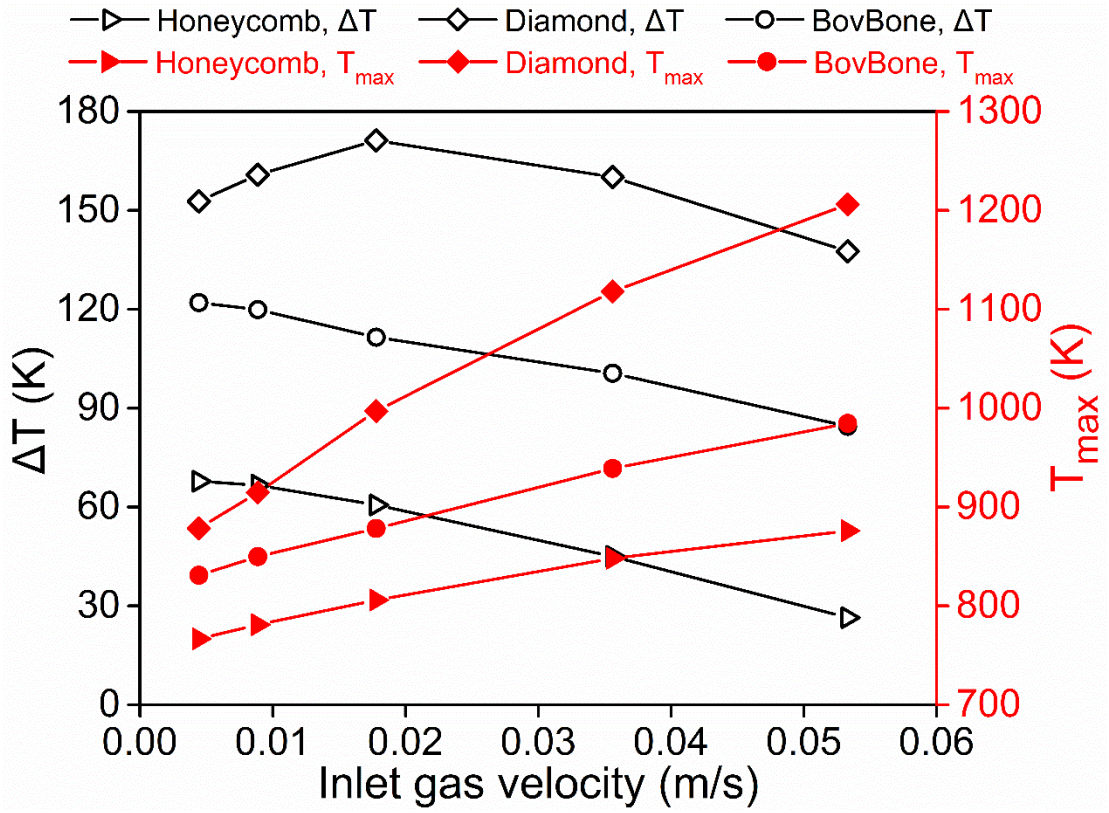
Honeycomb, ΔT
Diamond, ΔT
BovBone, ΔT
Honeycomb, T max
Diamond, T max
BovBone, T max
ΔT (K)
T max (K)
Inlet gas velocity (m/s)
0
30
60
90
120
150
180
700
800
900
1000
1100
1200
1300
0.00
0.01
0.02
0.03
0.04
0.05
0.06

FIGURE 10

(a)

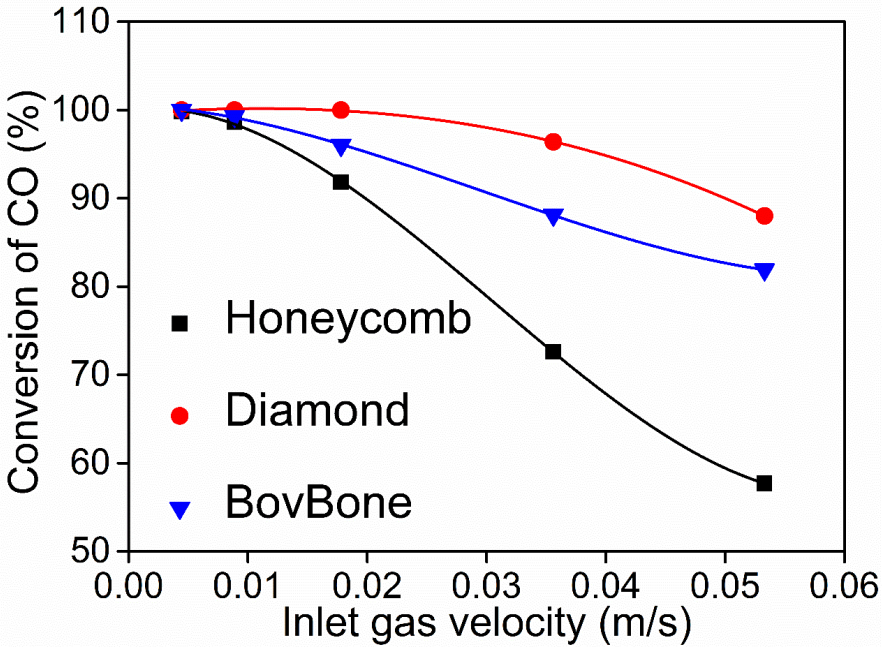
Conversion of CO (%)
110
100
90
80
70
60
50
0.00
0.01
0.02
0.03
0.04
0.05
0.06
Inlet gas velocity (m/s)
Honeycomb
Diamond
BovBone

(b)

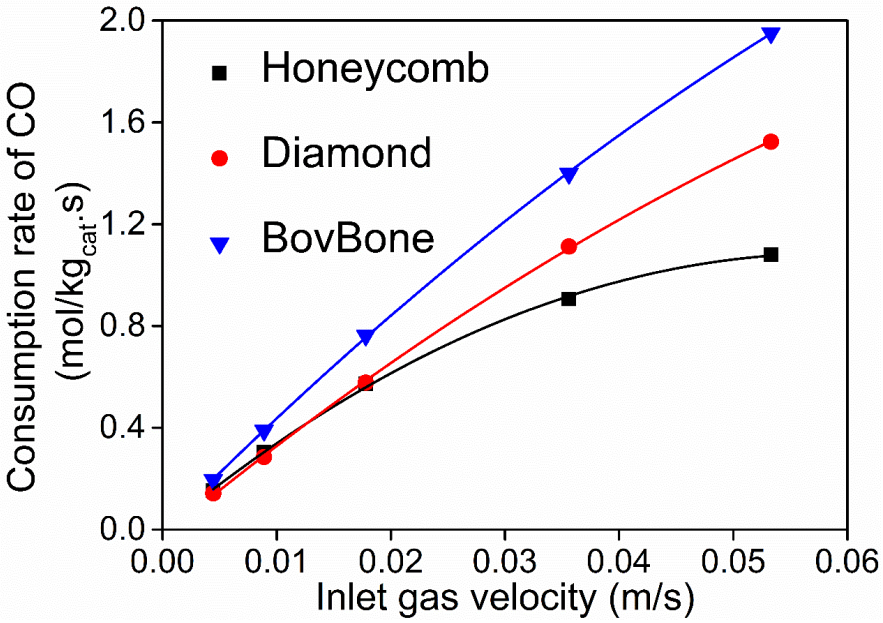
Consumption rate of CO
(mol/kg$_{cat}$.s)
2.0
1.6
1.2
0.8
0.4
0.0
0.00
0.01
0.02
0.03
0.04
0.05
0.06
Inlet gas velocity (m/s)
Honeycomb
Diamond
BovBone

FIGURE 11

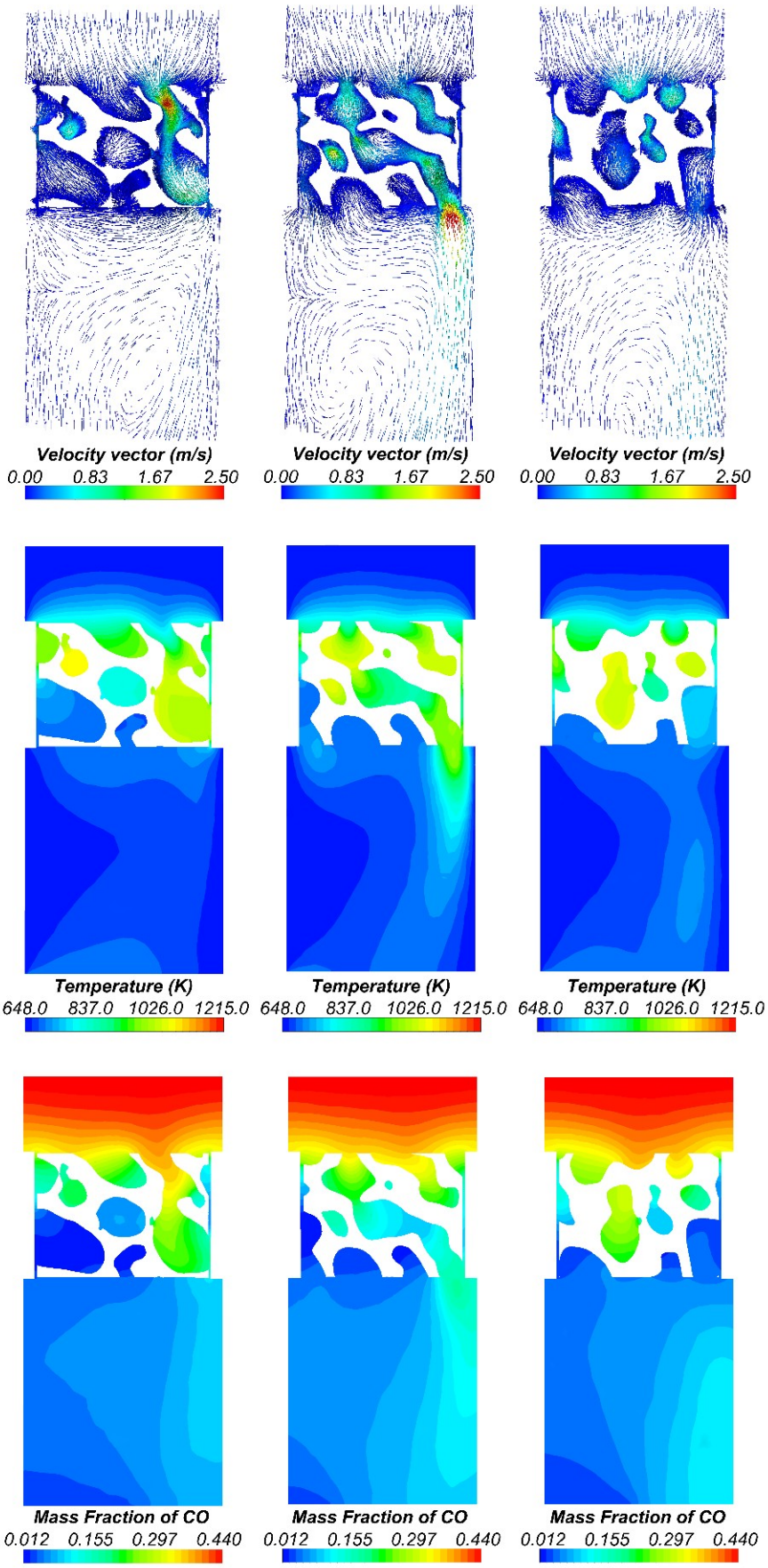
Velocity vector (m/s)
0.00 0.83 1.67 2.50
Velocity vector (m/s)
0.00 0.83 1.67 2.50
Velocity vector (m/s)
0.00 0.83 1.67 2.50
Temperature (K)
648.0 837.0 1026.0 1215.0
Temperature (K)
648.0 837.0 1026.0 1215.0
Temperature (K)
648.0 837.0 1026.0 1215.0
Mass Fraction of CO
0.012 0.155 0.297 0.440
Mass Fraction of CO
0.012 0.155 0.297 0.440
Mass Fraction of CO
0.012 0.155 0.297 0.440

Table 1.

Catalyst type	Porosity %	Specific surface area mm^{-1}	Hydraulic diameter mm
Honeycomb	27.1	2.1	0.18
Diamond	21.2	1.4	0.19
BovBone	42.7	1.6	0.47

Table 2.

Catalyst type	ΔT (K)		CO Conversion (%)	
	CFD simulation	Experiment	CFD simulation	Experiment
Honeycomb	26.4	35	58	57.4
Diamond	137.6	98	88	90.1